

Summary

In this work, integration PZT ($\text{Pb}[\text{Zr}_{0.52}\text{Ti}_{0.48}]\text{O}_3$) piezomaterial in silicon technology has been studied. To realize this integration Pulsed Laser Deposition technique has been used.

Oxide buffer layers are needed for epitaxial growth of electrode material and PZT. 8% yttria stabilized zirconia (YSZ, $\text{Y}_2\text{O}_3\text{-ZrO}_2$) and cerium oxide (CeO_2) were chosen as buffer layers because they have close lattice match with silicon and good chemical stability. Strontium ruthenate (SrRuO_3) was chosen because this oxide has a close lattice match with buffer layer materials and PZT.

Goal is to form an epitaxial multilayer with (001) orientations, i.e. stacking of materials with the same crystal orientations. The (001) orientation of the multilayer is necessary to obtain a maximum piezoeffect of the PZT. Epitaxy and growth problems of thin buffer films during pulsed laser deposition are emphasized.

Before starting pulsed laser depositions of buffer layers, amorphous silicon oxide is present on the surface of a silicon substrate that prevents an epitaxial relation of buffer layer material and silicon. YSZ can build in the oxygen atoms of this silicon oxide and grow with (001) orientation on silicon ($\text{Si}[001]\}/\text{YSZ}[001]$). The degree of this epitaxy can be controlled by varying deposition time in an oxygen deficient environment. Cerium oxide does not possess this unique feature and grows not in a (001) orientation but in a (111) orientation ($\text{Si}[001]\}/\text{CeO}_2[001]$).

The orientation of a grown SRO electrode on either YSZ (001) or cerium oxide (111), is not the expected (001) orientation rather an (110) orientation derived from a pseudo-cubic structure inside a larger SRO orthorhombic lattice ($\text{YSZ}[001]\}/\text{SRO}[110]$ or $\text{CeO}_2[111]\}/\text{SRO}[110]$).

For PZT, it is unlikely to grow (001) oriented on a bottom electrode that is (110) oriented, like SRO ($\text{SRO}[110]\}/\text{PZT}[110]$).

Table of contents

1. Introduction	3
2. Pulsed Laser Deposition	4
2.1 Principle of Pulsed Laser Deposition	4
2.2 Thin Film Deposition and Growth in Pulsed Laser Deposition	5
3. Materials Overview: Characteristics and Mechanisms	7
3.1 Silicon	7
3.1.1 Hydrogen fluoride etching of native silicon oxide	8
3.1.2 Initial oxidation of hydrogen-terminated silicon in ambient environment	9
3.1.3 Thermal oxidation of silicon	10
3.2 Yttria Stabilized Zirconia (Y_2O_3 - ZrO_2)	13
3.3 Cerium Oxide (CeO_2)	15
3.4 Strontium Ruthenate ($SrRuO_3$)	16
3.5 PZT ($Pb[Zr,Ti]O_3$)	17
4. Experimental	18
5. Results	20
5.1 Silicon	20
5.1.1 Native oxide vs. hydrogen terminated	20
5.1.2 Passive vs. active oxidation	21
5.2 YSZ Deposition	22
5.3 Cerium Oxide Deposition	25
5.4 SRO Deposition	27
5.4.1 Deposition on YSZ	27
5.4.2 Deposition on cerium oxide buffered with YSZ	28
5.5 PZT Deposition	29
5.5.1 Si YSZ SRO PZT	29
5.5.2 Si YSZ CeO_2 SRO PZT	31
6. Discussion	32
7. Conclusions & Recommendations	36
Dankwoord	38
References	39

1. Introduction

In MEMS technology, actuation is usually electrostatic. A limitation of these devices is the electrostatic instability. To meet requirements that are set nowadays, the need of another actuation principle is becoming more important.

One solution is the use of piezomaterials for actuators. There are many innovative ideas for the integration of piezomaterials on silicon technology. However, there is little knowledge of reliability and reproducibility for the integration of piezomaterials on silicon.

Therefore, the integration of a thin film of piezomaterial in silicon technology is studied in this work. As a piezomaterial, a solid solution of lead zirconate and lead titanate (PZT) is used, because this material offers the largest piezoeffect of all piezomaterials.

For a successful integration of PZT, silicon (001) and buffer layers are used to orient the crystal structure of PZT in the (001) direction for a maximum piezoeffect. In this work, cerium oxide and 8% yttrium stabilized zirconia are chosen as buffer layer materials. Both materials show good epitaxy with silicon. This epitaxy is related to the small mismatch between the crystal lattices of silicon and the buffer materials.

Further, a bottom electrode is needed to measure piezoeffects of PZT. Strontium ruthenate is chosen as bottom electrode for PZT because this oxide can continue an epitaxial crystalline orientation with chosen buffer layer materials.

To grow these materials into an epitaxial multilayer, the pulsed laser deposition technique (PLD) is used. It is advantageous for pulsed laser deposition to deposit oxides, because oxygen stoichiometry can be controlled.

X-ray diffraction (XRD) and transmission electron microscopy (TEM) are used to characterize the overall orientation of prepared multilayers. In addition atomic force microscopy (AFM) is used to characterize surfaces of deposited materials.

Chapter 2 will give a background about pulsed laser deposition. Chapter 3 will review materials characteristics of yttrium stabilized zirconia, cerium oxide, strontium ruthenate, and PZT. Chapter 4 discusses sample treatment and PLD-settings. Chapter 5 presents the achieved results and will be discussed in chapter 6. Chapter 7 concludes this work.

2. Pulsed Laser Deposition

Pulsed laser deposition is conceptually a simple technique involving the collection on a nearby substrate of material ejected (ablated) from a pulsed laser irradiated target.

It offers several advantages: material transfer from target to substrate is stoichiometric; it does not require an ultra-high vacuum environment; the gas environment can be changed and offers a broad pressure range, and multilayers are readily grown by irradiation of consecutive targets. Figure 2.1 shows a schematic PLD setup similar to the one used for the experiments in this work. The laser source is a KrF excimer laser with a wavelength of 248 nm (Lambda Physik Compex 201).

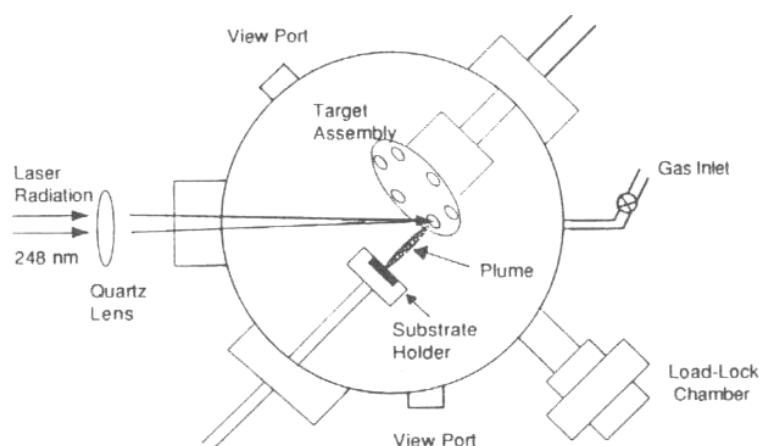


Figure 2.1: Schematic diagram of a PLD set-up. Load lock chamber is not present in actual used PLD system [2].

The PLD equipment used has some disadvantages: the film thickness uniformity is not optimum and the film area that can be deposited is relatively small ($\sim 10 \times 10 \text{ mm}^2$). Only three targets can be mounted into the PLD system used. To continue deposition with a fourth target, the PLD system has to be opened, and vacuum pumped again.

In the next chapters, the principle of PLD will be addressed, followed by the deposition and growth of thin films.

2.1 Principle of Pulsed Laser Deposition

As mentioned, material is ejected from an irradiated target: a laser beam is focused through a lens onto the target, a pulse of this beam (pulse length = 15-200 ns) results in evaporation of material from the target. The vapor above the target surface is further heated by absorption of the laser energy during the pulse and forms a plasma due to the very high temperatures reached (20,000-40,000 K) [4]. This layer expands perpendicular to the target, driven by a pressure gradient. This process is called ablation (figure 2.2). Important parameters for the *amount* of ablated material are the fluency (typically $1\text{-}3 \text{ J/cm}^2$), the spot size (typically $2\text{-}6 \text{ mm}^2$) of the incident laser beam and the density of the target itself [2].

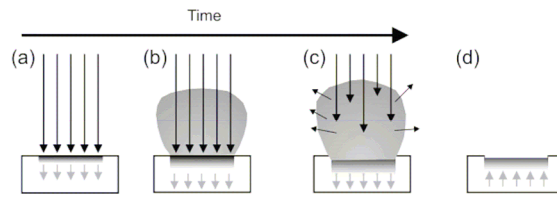


Figure 2.2: Schematic illustration of the ablation process. (a) Initial absorption of laser radiation, melting and evaporation begins. (b) Vaporization continues, plasma forms due to interaction of laser with evaporated material. (c) plasma continues to form, plume propagates driven by pressure gradient. (d) Melted material re-solidificates [1].

Before this ablation process starts, the PLD chamber must be vacuum pumped to replace the air in the chamber by pure oxygen or argon (the used PLD system has to be opened to remove or replace targets and substrates). The gas introduced before ablation in this vacuum is called the background gas. The type and pressure of the background gas are with the fluency and laser spot size important parameters of the ablation process, because the chosen gas determines the *shape* of the plasma plume (figure 2.3) and thus the *spreading* of ablated species in the plasma [2-5]. Higher gas pressures result in a smaller mean free path of ionized particles and other species in the plasma, which result in a narrower distribution of the plume. This is illustrated in figure 2.3. The same is applicable to the molecular or atomic weight of the background gas. A plume evolving in heavier gas molecules or atoms at the same pressure will result in a narrower distributed plume.

To collect the desired quantity of ablated material from this plasma, the distance between the ablated target and the substrate is an important parameter.

The oxygen stoichiometry of this ablated material can be influenced by changing oxygen gas pressure and oxygen gas flow. If needed, oxygen gas can be replaced by argon gas by the used PLD system.

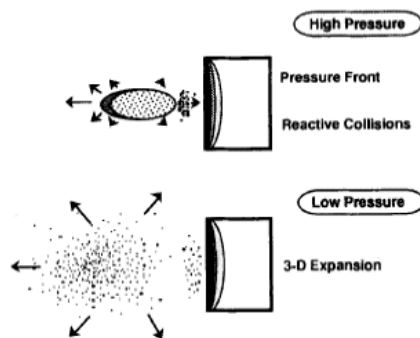


Figure 2.3: Pressure effects on plume distribution in PLD; after [4].

2.2 Thin Film Deposition and Growth in Pulsed Laser Deposition

During material ablation from target to substrate, atoms can adsorb on the surface of the substrate depending on their kinetic energy. This may involve a ‘gentle’ adsorption onto the surface or a violent embedding and damage of the pre-existing film. Larger particles may fragment on impact.

When the substrate-ablated atom interaction is strong enough, and the lattice mismatch between the lattice parameters of substrate and film is small enough, the crystalline orientation of the film can be controlled by the crystalline orientation of

the substrate: epitaxial growth. Providing substrate temperature is right for epitaxy [1].

Assuming a ‘gentle’ adsorption and epitaxial relation, figure 2.4 illustrates typical atomic processes on a perfect substrate surface of submonolayer growth.

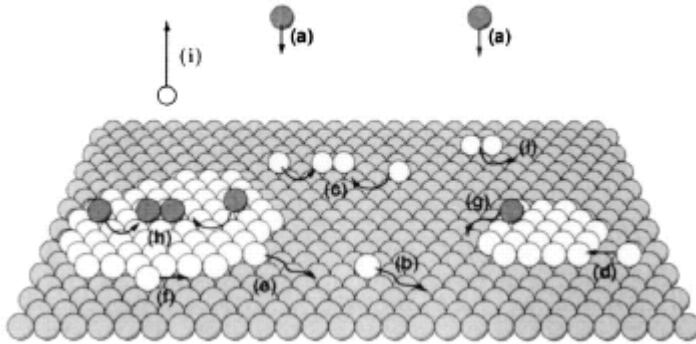


Figure 2.4: Typical atomic processes during epitaxial growth [6].

Atoms are deposited with a deposition flux F (a) Once on the surface, the atoms can diffuse (b). Adatoms can meet other adatoms (c), or attach to existing islands (d). Once an adatom is attached to an island they can detach from the island edge (e) or diffuse along the island edge (f). Corresponding processes of deposited adatoms on islands take place as well (g), (h); at high temperatures some adatoms can re-evaporate (i) [6].

3. Materials overview: Characteristics and Mechanisms

3.1 Silicon

In this work, p-type silicon (001) oriented substrate is used with a resistance of 2-10 $\Omega \text{ cm}^2$. The crystal structure of silicon is a cubic diamond structure with a lattice constant of 5.41 Å. Figure 3.1 illustrates the diamond structure of silicon.

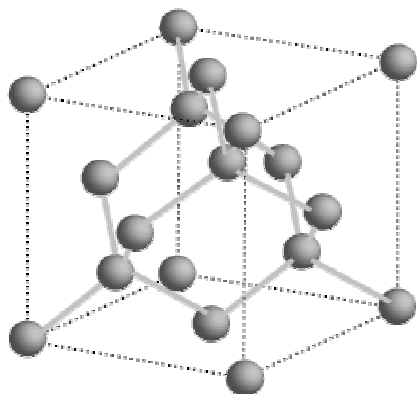


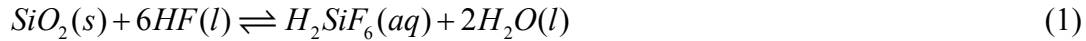
Figure 3.1: Cubic diamond structure of silicon (001).

Critical for epitaxial growth of a buffer layer is the crystalline quality of the silicon substrate. Silicon can oxidize readily into an amorphous layer of silicon oxide. During storage in air the substrates will oxidize inevitably, called native oxide. This oxide layer can prevent epitaxial growth of buffer layer material by PLD. Therefore, the silicon substrates are etched by a 1% hydrogen fluoride solution to remove native oxide. During transport in air of a silicon substrate to the PLD system and during heating at low pressures ($<10^{-5}$ bar) inside the PLD system, re-oxidation after etching is a possibility.

Because silicon oxidation is an important aspect for the integration of PZT on silicon technology, etching and oxidation mechanisms are reviewed.

3.1.1 Hydrogen fluoride etching of native silicon oxide

The dissolution of silicon dioxide by aqueous HF is based on the overall reaction [7,9]:



Although the mechanisms of silicon etching are not fully understood and other reactions could be possible [10,11], the removal of native silicon oxide is suggested to proceed stepwise according to reaction (1) and figure 3.2:

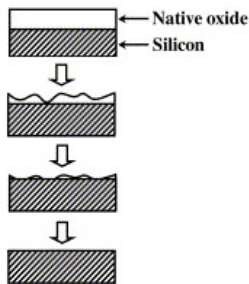


Figure 3.2: Possible etching steps of silicon (001) native oxide, after [12].

In low molarity hydrogen fluoride solutions, the native oxide layer is moderately etched. Etching of the oxide layer may occur non-uniformly due to difference in oxide thickness or lateral variations in oxide stoichiometry (SiO_x).

Although silicon (001) has a higher surface chemical reactivity than e.g. silicon (111) and (110) because more dangling bonds at the surface are present, the concentration of the HF solution used (1%) is sufficiently low to prevent surface roughening of the silicon during etching.

After two minutes in the HF-solution, the samples are rinsed in ultra-pure water followed by alcohol and dried with nitrogen to prevent further etching of the surface.

The surface of the silicon substrate is hydrogen terminated thus hydrophobic (figure 3.3). Hydrogen termination protects the silicon surface against oxidation. Although oxygen has a low sticking coefficient in respect to hydrogen terminated surfaces [13,14] (sticking coefficient $\approx 10^{-14}$ - 10^{-12}), attention should be paid to further processing the etched sample. Hydrogen termination makes it sensitive to hydrocarbon contamination, due to hydrophobic interactions [15].

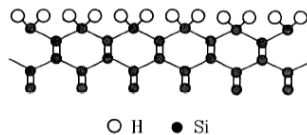


Figure 3.3: Hydrogen terminated silicon (001) surface [16].

3.1.2 Initial oxidation of hydrogen-terminated silicon in ambient environment

During rinsing with ultra-pure water (UPW), it is possible that hydrogen-terminated silicon oxidizes in the presence of dissolved oxygen [17-19]. For native silicon oxide to reform, water or water molecules are needed in addition to molecular oxygen [18-21]. Water or water vapor acts as a catalyst; therefore environmental humidity is a factor in silicon oxidation. To illustrate the influence of water, figure 3.4 shows a development of silicon oxide thickness for p-type and n-type bare silicon in an ambient environment (19 °C, 39% humidity). It can be seen that silicon oxidizes rapidly, forming a 2 Å thick native oxide layer almost immediately.

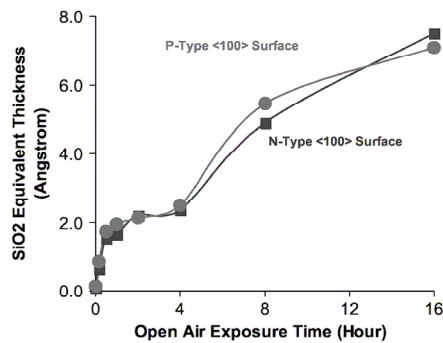
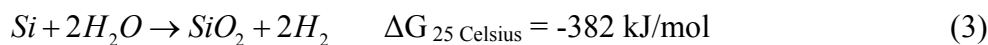
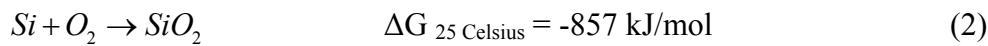


Figure 3.4: Oxidation of p-type vs. n-type wafer surfaces in time in open air at 19 °C and 39% humidity [18].

Based on thermodynamics, oxygen and water can both oxidize silicon to form SiO₂ according to the reactions [21]:



Both reactions have a negative free energy at room temperature and are thus spontaneous. It seems silicon oxidation is determined by kinetics rather than thermodynamics.

The mechanism of oxidation is thoroughly investigated in literature. The hydrogen terminated surface or Si-H bonds are stable against oxidation, but the Si-Si back bonds are significantly less stable and easier attacked by oxygen and water [22-26]. High-resolution electron energy loss spectroscopy (HREELS) and Fourier transform infrared spectroscopy (FTIR) studies revealed the formation of Si-O-Si back bonds at room temperature leaving Si-H bonds intact beneath surface oxygen coverage of 0.4 [24,25]. Higher oxygen coverage resulted in an oxidation similar to that of clean silicon surface. If all Si-Si backbonds are oxidized, oxidation can continue forming Si-OH on the surface [26]. Figure 4.4 shows a schematic drawing of the oxidation process.

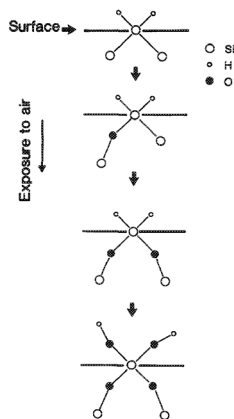


Figure 3.5: Structural changes of the hydrogen-terminated silicon surface in the initial stage of oxidation in air at room temperature [26].

3.1.3 Thermal oxidation of silicon

When the substrate has been mounted in the PLD chamber, the PLD chamber is vacuum pumped ($<10^{-5}$ bar). Heating of the substrate starts and oxidation of the silicon substrate will continue (even in a low oxygen concentration). During heating the hydrogen desorbs from the substrate surface at ~ 300 °C [20,24,25,27], making the silicon surface vulnerable to oxidation by oxygen and water.

During heating (300 °C \rightarrow 800 °C), when all the hydrogen atoms are desorbed, thermal oxidation of silicon is the main mechanism that forms silicon oxide. Figure 3.6 shows the general picture of silicon oxide formation with five distinct steps: sticking of oxygen molecules, incorporation, diffusion, reaction and growth of silicon oxide.

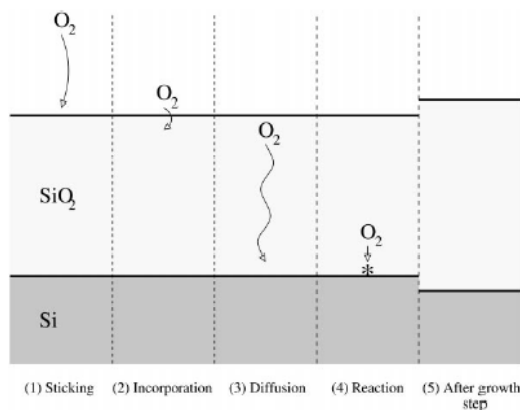
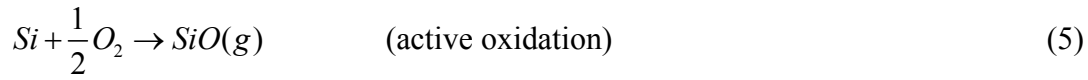


Figure 3.6: Evolution of the oxide as successive layers are added. The asterisk is a defect formed at the silicon/oxide interface and stays at the same distance from the oxide/gas interface.

Two mechanisms are suggested concerning thermal oxidation: Deal-Grove [28] and Mott-Cabrera [29]. In thick oxide layers (>30 nm) the Deal-grove mechanism dominates, which is based on a diffusion model created by a concentration gradient of oxygen at the gas/oxide interface and the oxide/silicon interface. For thinner layers (<3 nm), concentrations gradients are not important and electron tunneling is the major driving force for oxygen incorporation: the Mott-Cabrera mechanism. The electric field created by the electron transfer drives oxygen diffusion across the film and causes it to thicken, as mentioned in references [30,31].

At high temperatures and at low pressures, two regimes of silicon oxidation can dominate: the passive oxidation regime and the active oxidation regime. These oxidation regimes are characterized by the following equations [32,33];



Passive oxidation means the growth of oxide on the silicon surface; active oxidation is the evaporation of silicon mono-oxide from the surface. Which regime dominates for a particular temperature and pressure is depicted in figure 3.7.

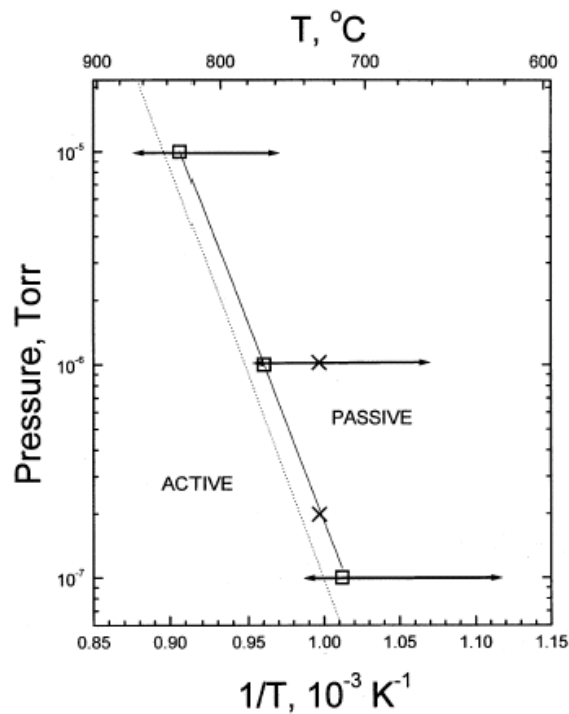


Figure 3.7: Phase diagram for silicon oxidation (solid line).

Calculations on Si-O bonding distances and relative energies show that the previously formed silicon-oxygen backbonds play an important role in the active oxidation region. A proposed mechanism is shown in figure 3.8. If an oxygen molecule adsorbs on the surface (a), it forms an on-dimer bond (e) or an on-top bond (b). The on-top bond shifts into a backbond (lower energy) (c) and causes the evaporation of SiO (etching in figure 3.8) (d). The on-dimer bond can relax to a more stable dimer-bond (f) due to the high temperature of the substrate (800 °C). This high temperature delivers enough energy to initiate bond switching (b-e or e-b), diffusion, nucleation and growth processes [32].

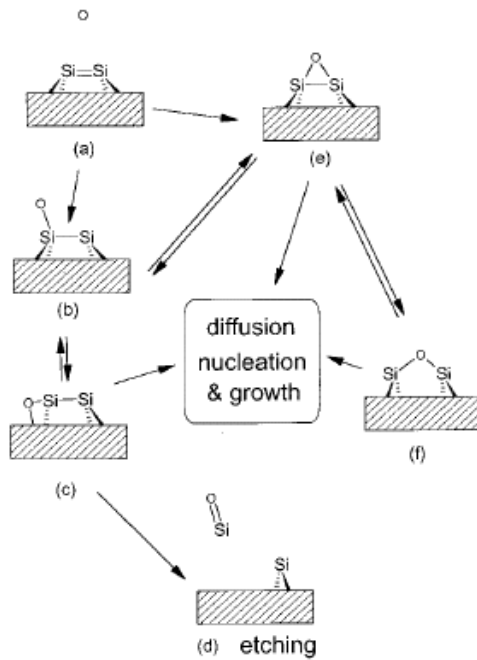


Figure 3.8: Proposed mechanism for the passive-active surface oxidation of silicon. Two bonds will form initially: on-top and on-dimer. The on-top structure is either converted into a backbond or on-dimer bond. The backbond is necessary to etch (active oxidation) the surface [32].

It is difficult to predict the rate (the silicon oxidation rate is determined by kinetics) at which silicon oxide forms. Oxide thickness and growth mode during heating for this particular process inside the PLD chamber are unknown too. The proposed mechanism for active-passive growth of silicon oxide can definitely be present during heating in background pressure.

Considering the oxidation processes described above, Si-O bonds will probably always form before deposition of buffer layer material. This fact has to be taken into consideration while growing epitaxially on silicon substrates.

3.2 Yttria stabilized Zirconia ($\text{Y}_2\text{O}_3\text{-ZrO}_2$)

In this work a zirconia target with 8% yttria content is used for deposition. The crystal structure of 8% YSZ is a cubic fluorite structure with a lattice constant of 5.14 Å.

Figure 3.9 illustrates the fluorite structure of YSZ.

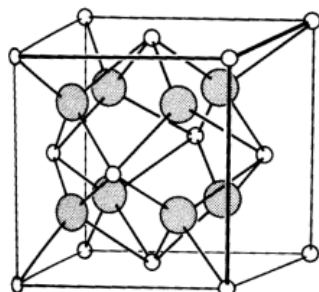


Figure 3.9: Fluorite structure of 8% YSZ.

The reasons to use YSZ are 1) small lattice mismatch in respect to silicon: 5%, so epitaxial growth is possible; 2) during deposition YSZ in an oxygen deficient environment, it can function as a silicon oxide ‘scavenger’. It can incorporate the oxygen of the silicon oxide into its own lattice, which can be helpful because there is a strong indication that silicon oxide has formed before any deposition is started (paragraphs 3.1.2 & 3.1.3). According to the following reactions, ‘oxygen scavenging’ is possible [34-40]:



Figure 3.10 illustrates the proposed growth process of ZrO_2 (YSZ) thin films under $1.3 \cdot 10^{-5}$ bar O_2 and 900 °C.

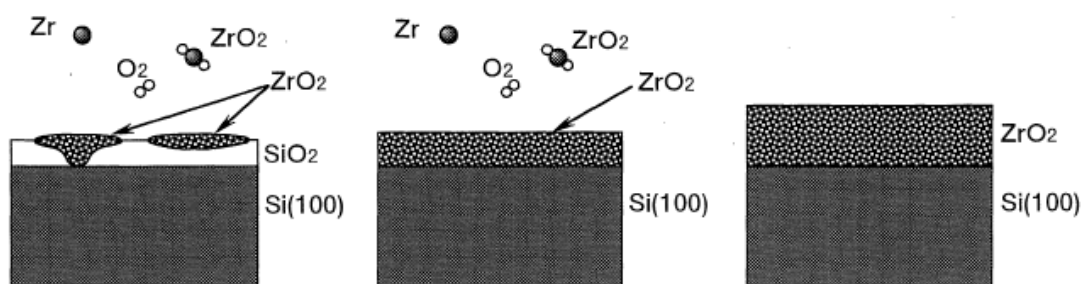


Figure 3.10: Proposed initial growth process of YSZ under $1.3 \cdot 10^{-5}$ bar oxygen pressure and 900 °C [37].

Frequently, an oxide layer is reported between the silicon-YSZ interface. It is postulated that this re-growth of silicon oxide is due to the high O^{2-} ion conductivity of YSZ at elevated temperatures and O_2 gas exposure during film growth or cooling of the samples [41]. This ion conductivity can be ascribed to oxygen vacancies in the zirconia by the introduction of yttria:



The oxide re-growth does not need to interfere with epitaxy of the grown YSZ film. As the YSZ film thickens, the substrate epitaxial influence is quickly lost, so oxide re-growth can occur as long as the grown oxide does not exceed the strain limit of the film (silicon oxide takes up a larger volume per mole than ordinary silicon, about 120%).

On the other hand, if the silicon oxide layer between silicon and YSZ is thin enough (~1-1.5 nm) it is suggested it can relax the strain between YSZ and silicon. [41,42]. This strain can be introduced by lattice mismatch or the large discrepancy in thermal expansion coefficients (YSZ: $\sim 10 \times 10^{-6}$; Si: $\sim 4.5 \times 10^{-6}$).

3.3 Cerium Oxide (CeO₂)

The crystal structure of cerium oxide is a cubic fluorite structure (see figure 3.9) with a lattice constant of 5.41 Å, thus matching silicon almost exactly (misfit ~0.4%).

Although this almost perfect match, often cerium oxide (011) [43-46] or (111) [47-49] is reported rather than cerium oxide (001). One reason for this unfortunate relation between cerium oxide and silicon is the amorphous silicon oxide, formed on the silicon (paragraphs 3.1.2 & 3.1.3). A two dimensional cerium atom population is highest in the (111) plane; the higher Coulombic interaction between cerium and oxygen should favor the CeO₂ (111) growth. In addition, cerium oxide does not possess the unique 'oxygen scavenging' feature like YSZ.

When ceria is deposited on an oxide-free silicon (001) surface, it is assumed the dangling free bonds of silicon interact preferentially with the oxygen in the Ce-O species, arranging the ceria in the (011) orientation rather than (001).

Besides YSZ, it is also possible for cerium oxide to transport oxygen ions through the deposited layer. Observed silicon oxide growth between silicon and cerium oxide can be explained in this way [45].

During deposition, the oxygen pressure is an important parameter to ensure growth of cubic cerium oxide. Only a slight discrepancy in the stoichiometry of cerium and oxygen, and a new phase is introduced, see figure 3.11. This δ -phase is not a cubic fluorite structure but an amorphous phase.

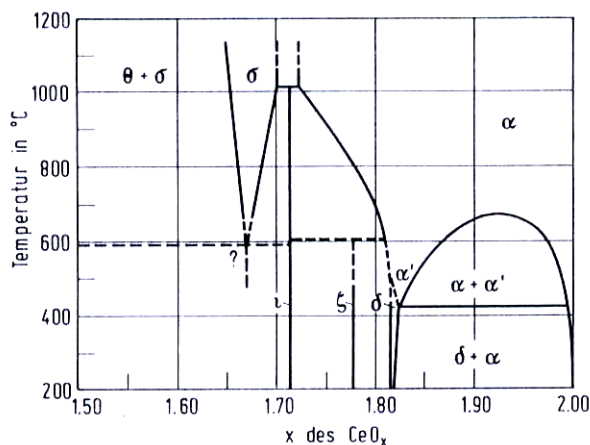


Figure 3.11: Phasediagram cerium oxide between CeO_{1.5} and CeO₂. The cubic fluorite phase is always formed when stoichiometry is correct. Between CeO_{1.818} en CeO₂, two phases exist simultaneously [50].

3.4 Strontium Ruthenate (SrRuO_3)

The crystal structure of strontium ruthenate (SRO) is orthorhombic, with a distorted perovskite structure, due to tilted RuO_6 octahedra (at RT), with lattice parameters of $a=5.57$, $b=5.53$, and $c=7.84$ Å. A structure transition to the tetragonal phase occurs at 550 °C and a transition to a cubic perovskite structure occurs at 680 °C [51]. Note that SRO can be considered as a pseudo-cubic perovskite structure with a lattice constant of 3.92 Å, also indicated in figure 3.12.

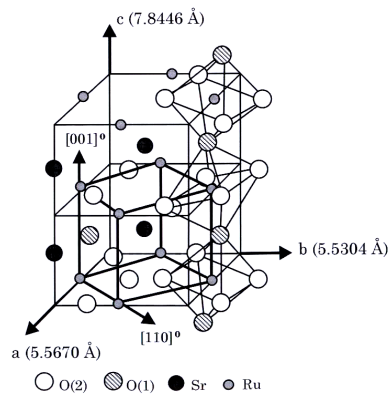


Figure 3.12: Orthorhombic symmetry with a distorted perovskite structure [51]

In contrast to YSZ and cerium oxide, which function as a buffer layer, SRO is the electrode of the system. An epitaxial rectangle-on-cube relation is reported [52-55]. The relation between SRO, YSZ and silicon can be described as $\text{SRO}[110]/\text{YSZ}[001]/\text{Si}[001]$. The SRO (110) plane is based on the pseudo-cubic structure of the SRO lattice. Figure 3.13 shows a schematic drawing of the rectangle-on-cube relation of SRO and YSZ.

Its chemical stability is preserved over a wide temperature range and a high resistance to chemical corrosion and high conductivity makes it an excellent electrode.

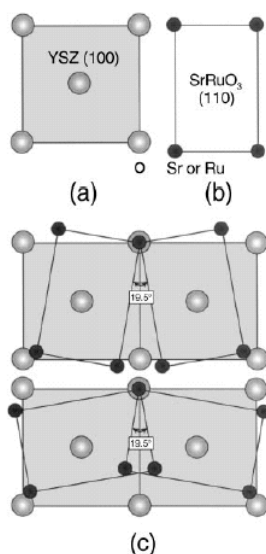


Figure 3.13: Schematic drawing of the rectangle-on-cube epitaxy of SRO on YSZ; a) (100) plane of YSZ; b) (110) plane of SRO (pseudo-cubic!!); c) four variants of the epitaxial rectangle-on-cube relationship of SRO on YSZ [54].

3.5 PZT (Pb[Zr,Ti]O₃)

PZT is a solid solution of PbZrO₃ and PbTiO₃. In this work a mixture with ratio Pb(Zr_{0.48}Ti_{0.52})O₃ is used. This material has rhombohedral ($a=b\neq c$; $\alpha=\beta=\gamma\neq 90^\circ$, $<120^\circ$) or tetragonal ($a=b\neq c$; $\alpha=\beta=\gamma=90^\circ$) perovskite structure depending on the ratio of the solid solution (see figure 3.14 and 3.15). Due to an asymmetry in these structures, the material is piezo-/ferroelectric. The cubic phase is symmetrical and is called paraelectric i.e. it is not piezo-/ferroelectric.

The line indicating a separation between the rhombohedral and tetragonal phase is called the morphotropic phase boundary (MPB). The piezoeffect is largest around or on the MPB. This piezoeffect, or piezoresponse, is caused by an applied electric field or applied stress. When an electric field (+ or -) is applied the material is polarized, resulting in strain in the material and a change in dimension (they contract or expand): the *converse* piezoelectric effect. If stress is applied, the material will be polarized as well, but this results in an electric field (or current when connected with a read-out device): the *direct* piezoelectric effect.

It is claimed that this large piezoeffect is caused by the introduction of a monoclinic phase under ~ 300 K [56].

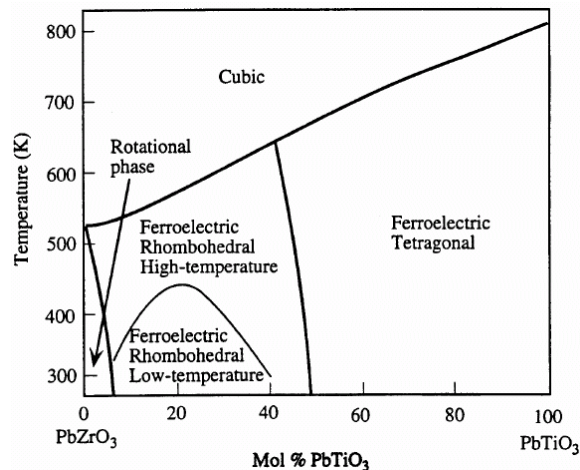


Figure 3.14: The morphotropic phase boundary after Jaffe *et al* [57].

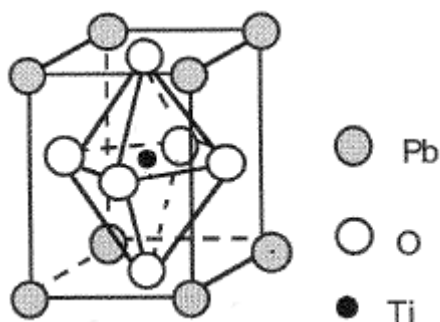


Figure 3.15: Tetragonal piezoelectric/ferroelectric phase of PZT, after [58].

4. Experimental

This chapter will give an overview of etching procedures of the silicon substrate, PLD settings and characterization methods.

Etching

A p-type silicon wafer with resistance of 2-10 $\Omega \text{ cm}^2$ is cut into substrates of 5×5 mm².

Substrates are etched in a 1% HF-solution (Merck) during two minutes in an ultrasonic bath. After etching the substrates are rinsed with ultra-pure water and ethanol in this order. After rinsing the substrates are blow-dried with N₂, transported to the PLD-chamber and mounted onto the heater.

Pulsed laser deposition

Targets are polished until no traces of previous ablations are visible, before mounting into the rotating target holder. Targets are pre-ablated.

Laser: Lambda Physik Compex 201
KrF excimer laser, wavelength = 248 nm, pulse duration = 50 ns

Deposition parameters:

Target:	CeO ₂	YSZ (8%)
Substrate:	Si(001)	Si(001)
Substrate temperature:	550 °C	800 °C
Background pressure:	<10 ⁻⁵	<10 ⁻⁵
Laser fluency:	1.2 J/cm ²	2.1 J/cm ²
Laser frequency:	2Hz	7 Hz
Spot size:	~5.9 mm ²	~3.4 mm ²
Pre-ablation:		
Time:	1 min	2 min
Pressure:	0.1 mbar	0.1 mbar
Ar-flow:	10 ml/min	10 ml/min
Deposition:		
Ar-time:	1-6 min (16-100 nm)	0-1 min (0-10 nm)
Ar-pressure:	0.100 mbar	0.021 mbar
Ar-flow:	10 ml/min	8 ml/min
O ₂ -time:	6 min (~100 nm)	10 min (~100 nm)
O ₂ -pressure:	0.1 mbar	0.021 mbar
O ₂ -flow:	10 ml/min	10 ml/min
Target-substrate distance:	45 mm	59 mm
Ramp-rate:	4 °C/min	---

Target:	SRO	PZT
Substrate:	Si(001)	Si(001)
Substrate temperature:	600 °C	600 °C
Background pressure:	N/A	<10 ^{-5*}
Laser fluency:	2.5 J/cm ²	3-6 J/cm ²
Laser frequency:	4 Hz	10 Hz
Spot size:	1.9 cm ²	3.0 cm ²
Pre-ablation:		
Time:	2 min	1 min
O ₂ -pressure:	0.13 mbar	0.1 mbar
O ₂ -flow:	15 ml/min	10 ml/min
Deposition:		
Time:	30 min (100 nm)	10-30 min (100-300 nm)
O ₂ -pressure:	0.13 mbar	0.1 mbar
O ₂ -flow:	15 ml/min	10 ml/min
Target-substrate distance:	49 mm	47 mm
Ramp-rate:	4 °C/min	---

*: PZT deposition is performed ex-situ.

Characterization

XRD: Single-crystal diffractometer, CAD4, Enraf Nonius Delft: Diffractis 586, CuK_α source.

TEM: Philips CM30

AFM: Digital Instruments, Nanoscope IV, contact mode.

5. Results

5.1 Silicon

5.1.1 Native oxide vs. hydrogen-terminated

The etched surface of a silicon substrate can be characterized by measuring the roughness with AFM. Figure 5.1 shows a hydrogen-terminated surface of a silicon substrate, etched in 1% HF solution.

The difference in hydrophobicity of a native silicon oxide surface and a hydrogen-terminated surface was measured with an advancing contact angle of demineralized water. Figures 5.2 and 5.3 show a native silicon oxide layer and a hydrogen-terminated surface respectively. The contact angle measured for a native silicon oxide layer is 37° . The contact angle of a hydrogen-terminated surface is 83° .

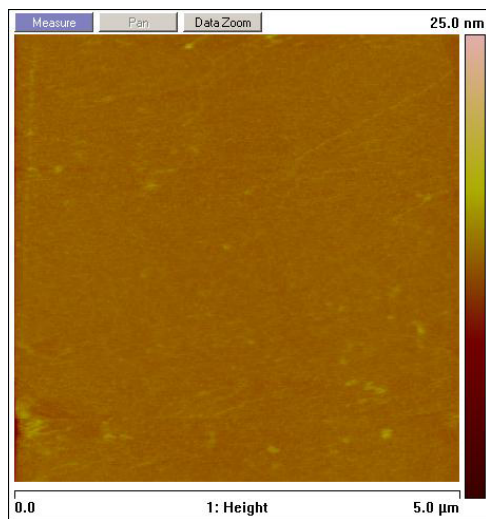


Figure 5.1: Silicon surface after etching with 1% HF solution (measured after 45 minutes in 21 °C and 40% humidity environment).

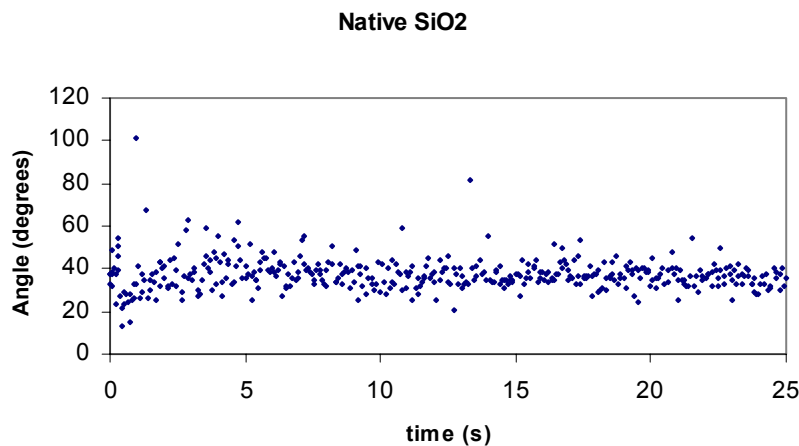


Figure 5.2: Advancing contact angle measurement of native silicon oxide.

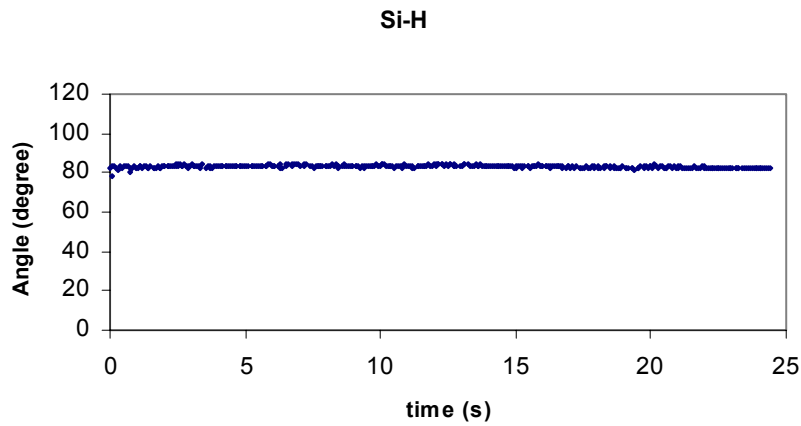


Figure 5.3: Advancing contact angle measurement of hydrogen terminated silicon; measured after one hour in ambient environment.

5.1.2 Passive vs. active oxidation

A contact angle measurement was performed on an etched silicon substrate that was heated to 800 °C and cooled without ramp-rate at a pressure of 8×10^{-6} bar. The contact angle is an average value of 42°, see figure 5.4.

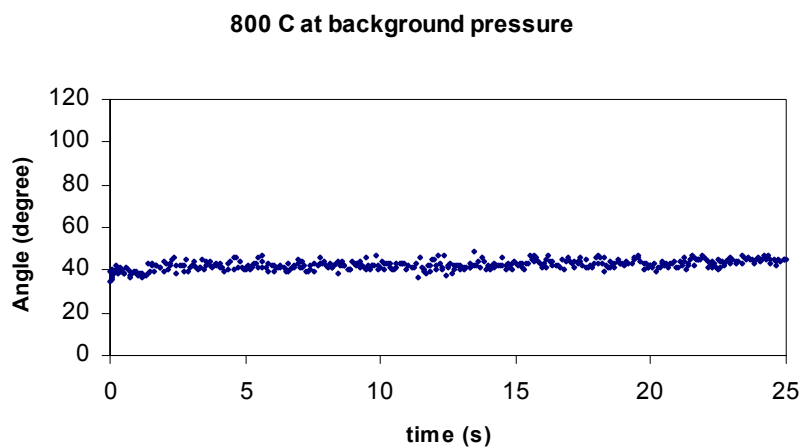


Figure 5.4: Advancing contact angle measurement of a heated substrate at 800 °C at 8×10^{-6} bar.

5.2 YSZ Deposition

The amount of deposited YSZ needed for oxygen scavenging can be controlled by deposition time in an argon environment. Samples with deposition times of 12, 24, 36, 48, and 60 seconds in an argon environment were prepared. The samples were characterized by XRD, TEM, and AFM. Figure 5.5 shows an optimum of (002) and (004) reflections in XRD measurements at 24 seconds. All samples were normalized to the intensity of the silicon substrate. Total deposition time in argon and oxygen is ten minutes to maintain the same thickness of YSZ layers (100 nm). Individual XRD measurements of a sample deposited for 24 and 48 seconds in an argon environment are presented in figure 5.6.

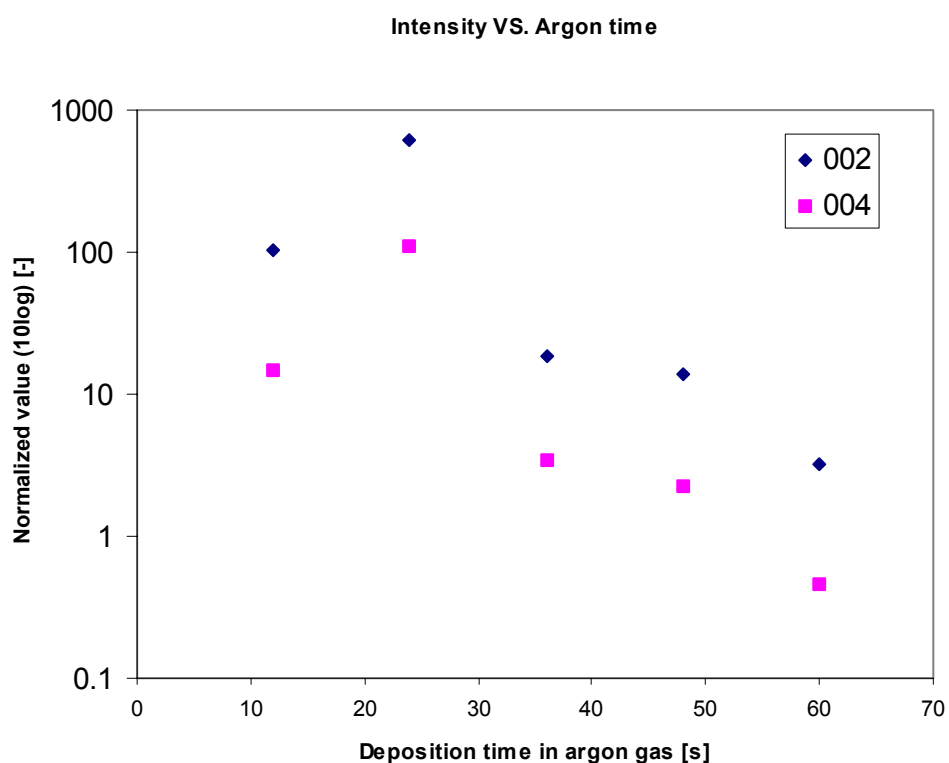
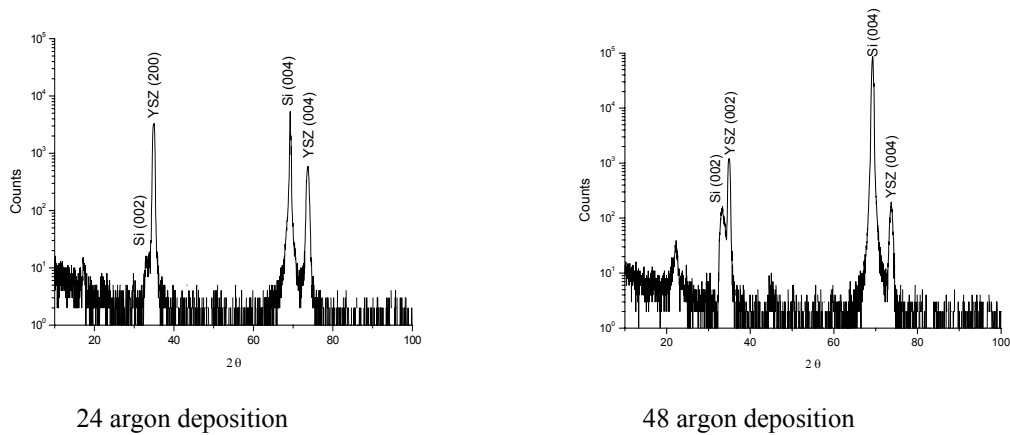
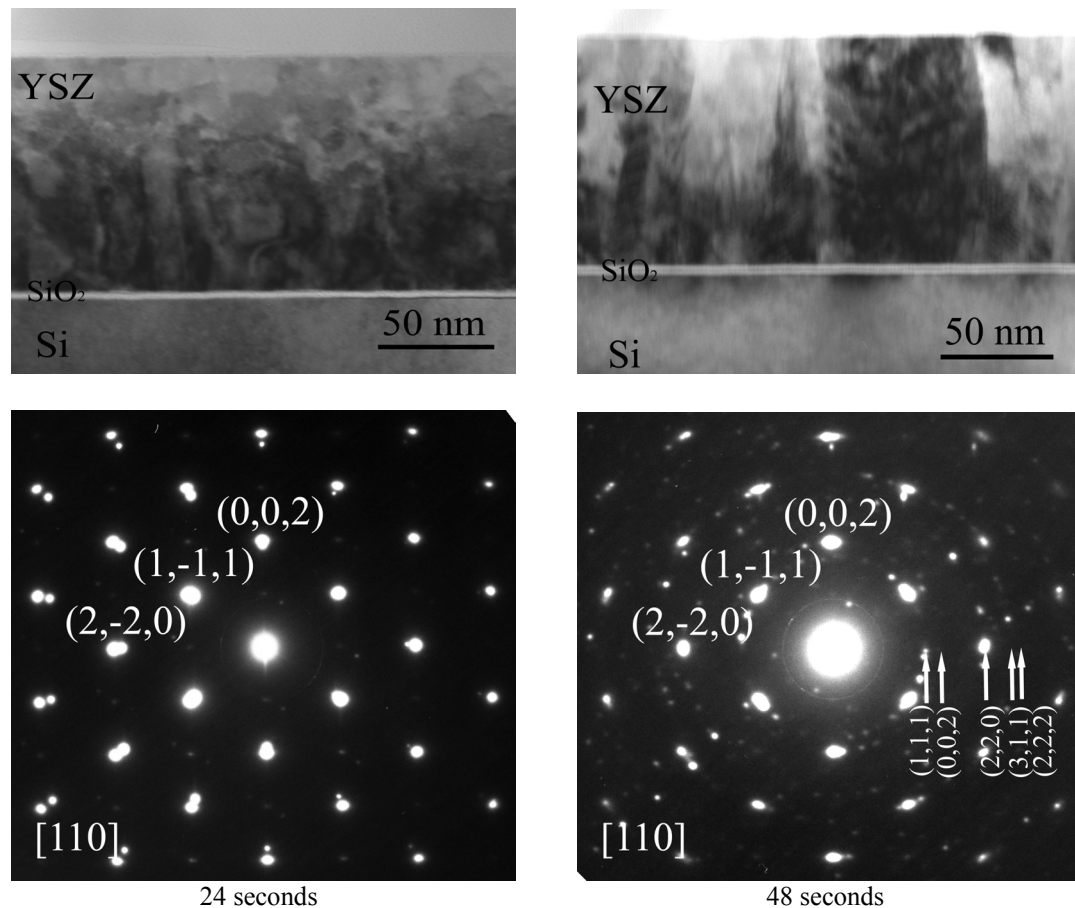


Figure 5.5: YSZ intensities normalized to silicon intensities versus deposition time of YSZ in argon gas. Note the logarithmic y-axis.



24 argon deposition
48 argon deposition
Figure 5.6: XRD measurements of a 24'' argon deposition and a 48'' argon deposition.

Further investigations of the individual presented samples with TEM show a dependence of crystalline orientations of YSZ with different argon deposition times, see figure 5.7. Dark areas in the upper pictures are (001) oriented. In the diffraction patterns beneath, the diffraction pattern of the 24-second argon sample is overlapping silicon (001) reflections (Si[001]/YSZ[001]). The 48-second argon sample shows different orientations besides (001).



24 seconds
48 seconds
Figure 5.7: TEM cross-sections and diffractions in [110] direction of silicon. Left) Cross-section and diffraction pattern of 24'' argon sample respectively; Right) Cross-section and diffraction pattern of 48'' argon sample respectively.

HREM pictures show a silicon oxide layer between the deposited YSZ and the silicon sample. The thickness of the 24-second argon and 48-second argon samples are 3 nm and 2.9 nm respectively

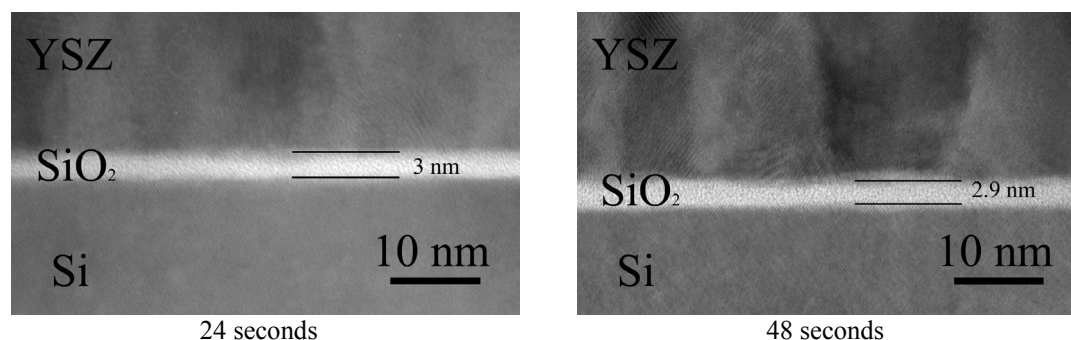


Figure 5.8: Silicon oxide thickness measured with HREM. Left) 24'' argon deposited YSZ layer; Right) 48'' argon deposited YSZ layer.

In addition, surface images were taken with AFM of the 24-second and 48-second argon samples. Both samples do not appear to be rough, although differences in height are detectable.

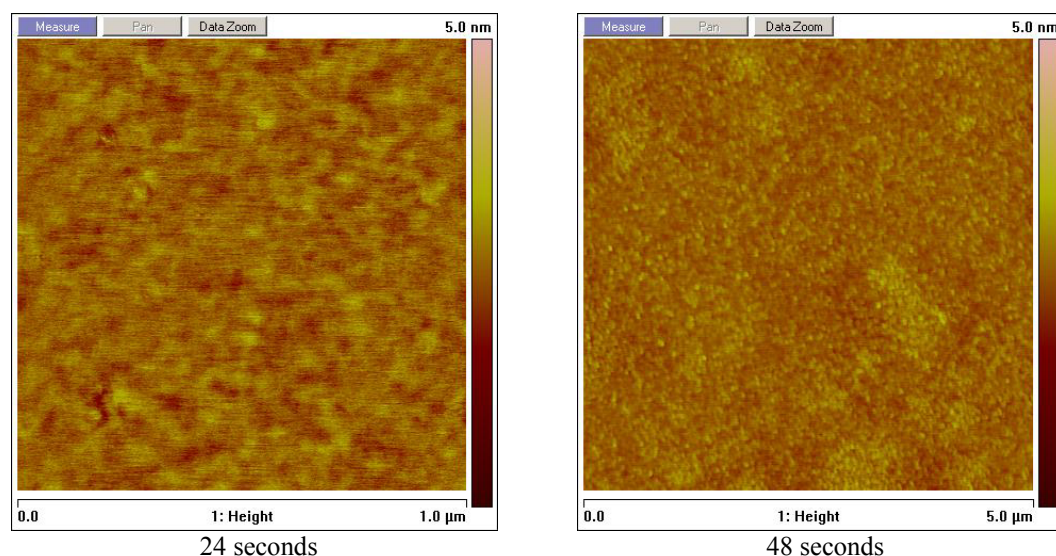


Figure 5.9: AFM pictures of YSZ surfaces. Left) AFM picture of YSZ layer deposited 24'' in an argon environment and 9'36'' in oxygen. Right) AFM picture of YSZ layer deposited 48'' in an argon environment and 9'12'' in oxygen.

5.3 Cerium Oxide Deposition

A Cerium oxide deposition was performed for six minutes in an argon environment. A second deposition was performed for one minute in an argon environment followed by an in-situ deposition of five minutes in an oxygen environment. A third deposition was performed for six minutes in an oxygen environment. All three samples were measured with XRD, showing a Si[001]//CeO₂[111] relation. See figure 5.10 A, B, and C respectively.

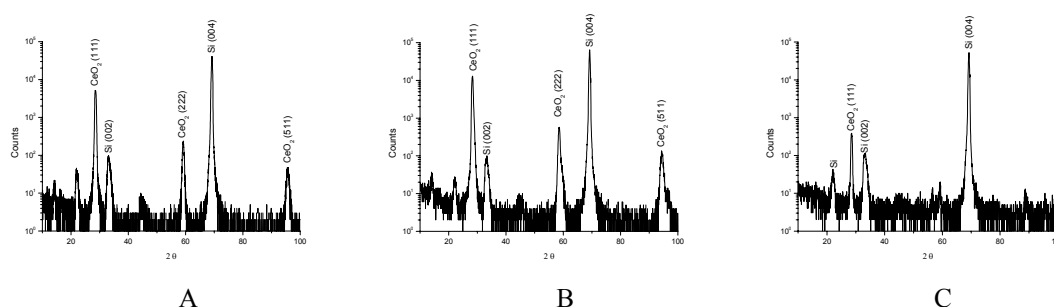


Figure 5.10: XRD measurements of cerium oxide deposited in different environments. A) 6' argon; B) 1' argon + 5' oxygen; C) 6' oxygen.

Further investigation of the argon deposited sample with TEM show a small silicon oxide layer between silicon and cerium oxide in figure 5.11. The diffraction pattern shows a (111) relation of cerium oxide with silicon. The spots marked with circles indicate silicon (001) orientation. The rest indicate cerium oxide (111) orientation.

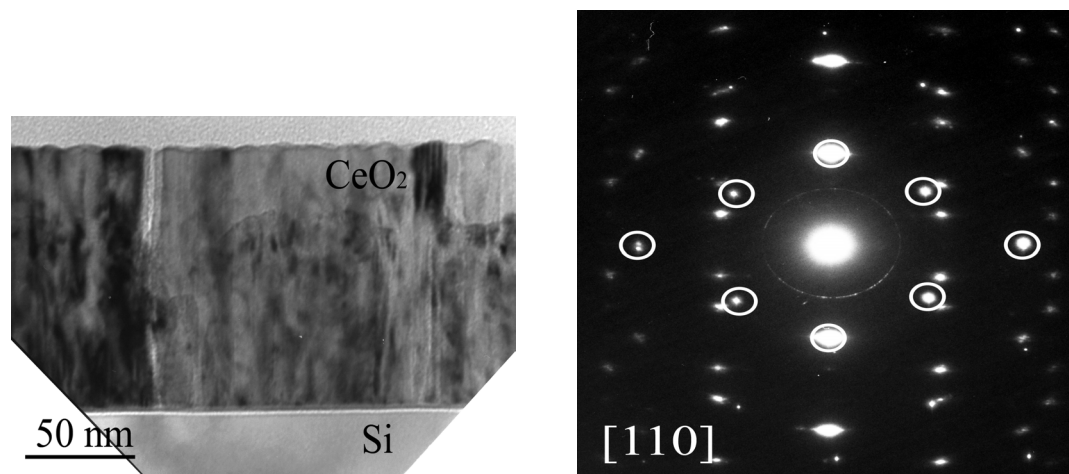
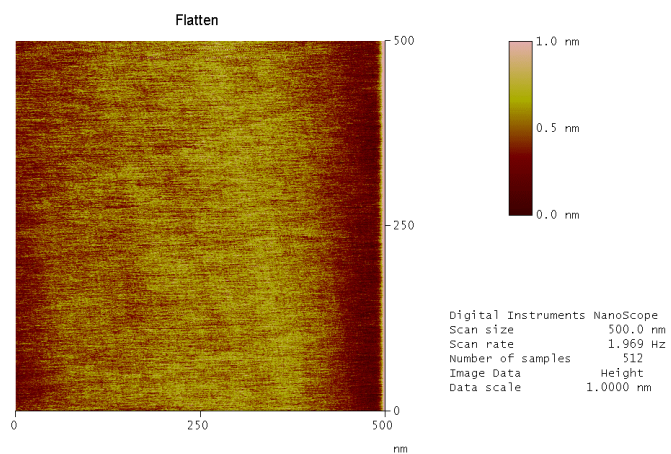


Figure 5.11: Left) TEM cross-section of a cerium oxide layer. Target-substrate surface = 42 mm. Right) TEM diffraction pattern of a cerium oxide layer.

Surface images taken with AFM show a very smooth surface of cerium oxide deposited layers. Figure 5.12 shows an AFM image of a cerium oxide layer deposited for six minutes in an oxygen environment.



ceo2_testrun1.001

Figure 5.12: AFM picture of CeO_2 deposited for six minutes in an oxygen environment. Note that these pictures are taken with Nanoscope III software.

5.4 SRO deposition

5.4.1 Deposition on YSZ

An in-situ deposition of SRO was performed on a pre-deposited 100 nm thick YSZ layer. The YSZ layer included a 24 seconds deposition in an argon environment. Figure 5.13 shows a Si[001]//SRO[110]_{cubic} or Si[010]//SRO[001]_{orthorhombic} relation. The 2θ value of the SRO peaks indicates a cell parameter of 3.93 Å.

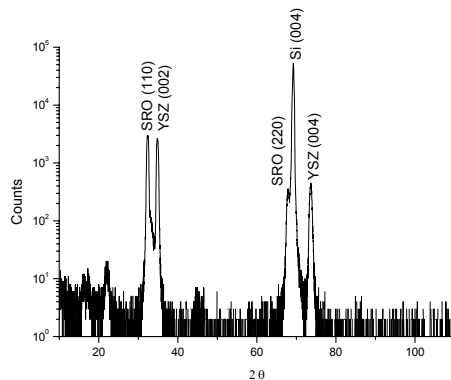


Figure 5.13: XRD measurement of SRO electrode deposited on 24'' argon time epitaxial YSZ layer.

An AFM measurement of the surface of this sample indicates a rough surface. Differences in height can be as high as eight nanometers. The line in the upper picture of figure 5.14 indicates the direction and area of the cross-section.

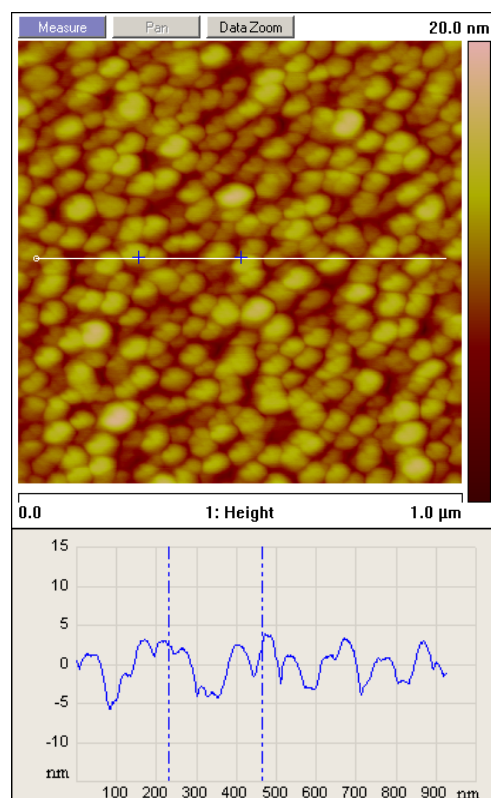


Figure 5.14: AFM measurements of a 100 nm thick SRO electrode on a pre-deposited 100 nm thick YSZ layer.

5.4.2 Deposition on cerium oxide buffered with YSZ

An in-situ deposition of SRO was performed on a pre-deposited cerium oxide layer buffered with YSZ. The YSZ layer included a 24 seconds deposition in an argon environment. Figure 5.15 shows a Si[001]//SRO[110]_{cubic} or Si[010]//SRO[001]_{orthorhombic} relation. As in paragraph 5.4.1, the 2θ value of the SRO peaks indicates a cell parameter of 3.93 Å. Cerium oxide peaks cannot be seen in this graph. AFM data is not available.

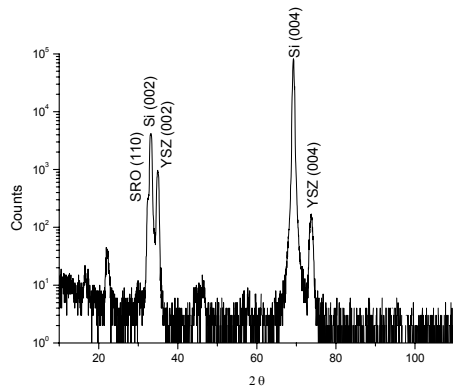


Figure 5.15: XRD measurement of a Si|YSZ|CeO₂|SRO multilayer.

5.5 PZT Deposition

5.5.1 Si | YSZ | SRO | PZT

A multilayer of YSZ | SRO | PZT on silicon has been prepared in-situ. The YSZ layer included a 24 seconds deposition in an argon environment, but a longer oxygen deposition time than mentioned in chapter 4. The YSZ layer is for this sample 300 nm. Figure 5.17 shows a Si[001]//PZT[110] relation.

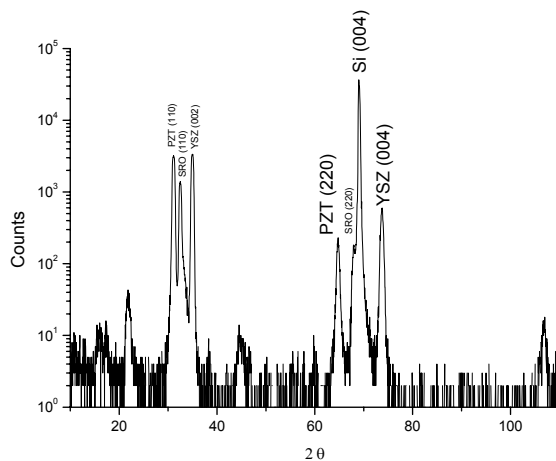


Figure 5.17: XRD measurement of PZT on SRO|YSZ|Si epitaxial multilayer.

Further investigation of this sample with TEM, shows a good epitaxial relation between SRO and PZT. In figure 5.17, grains within the SRO layer are continued through the PZT layer. PZT itself shows a columnar growth. The TEM diffraction pattern shows an (001) oriented YSZ plane. The arrows indicate a SRO and PZT plane, which are parallel to the [110] plane of silicon.

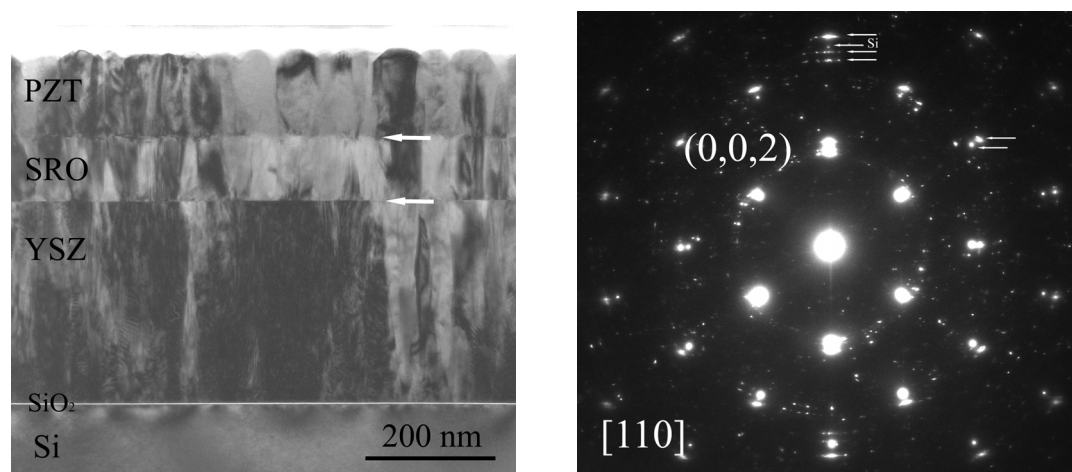


Figure 5.17: TEM cross-section and diffraction pictures from a Si|YSZ|SRO|PZT layer.

The surface of PZT is measured with AFM. Figure 5.18 shows a rough PZT surface together with a cross-section. The line in the upper picture of figure 5.18 indicates the direction and area of the cross-section.

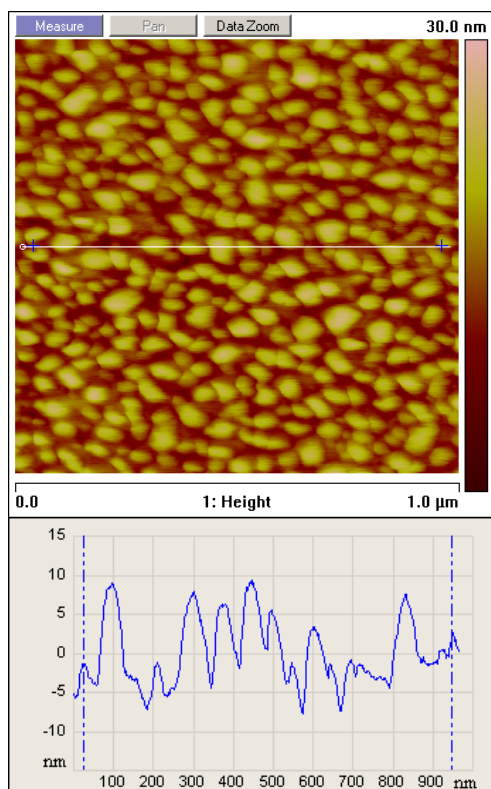


Figure 5.18: AFM measurement of a PZT surface deposited on a Si|YSZ|SRO multilayer.

5.5.2 Si | YSZ | CeO₂ | SRO | PZT

A multilayer of YSZ | CeO₂ | SRO on silicon has been prepared in-situ. The YSZ layer included a 24 seconds deposition in an argon environment. A PZT deposition was performed ex-situ. PZT layer has a thickness of 300 nm. Figure 5.19 shows a Si[001]//PZT[110] relation. Cerium oxide peaks cannot be seen in this graph.

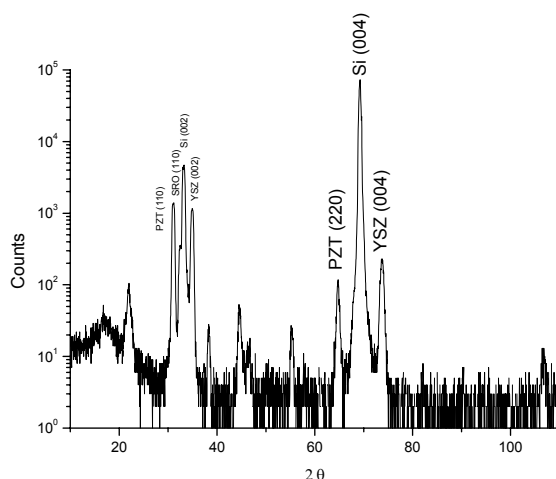


Figure 5.19: XRD measurement of PZT deposited on a Si|YSZ|CeO₂|SRO multilayer.

Further investigation of this sample with TEM, shows a good epitaxial relation between SRO and PZT. In figure 5.20, grains within the SRO layer are continued through the PZT layer. PZT itself shows a columnar growth. Cerium oxide and YSZ seem indistinguishable.

No AFM data is present, but the top of the PZT surface shows larger contours than in figure 5.17

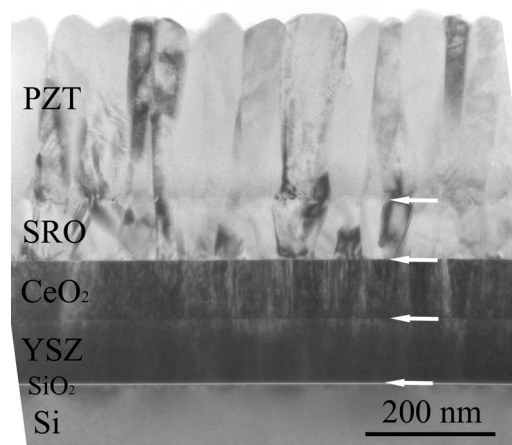


Figure 5.20: TEM cross-section of a Si|YSZ|CeO₂|SRO|PZT multilayer.

6. Discussion

Silicon oxide

Native silicon oxide is present on the surface of a wafer or sample. Etching with 1% HF solution is therefore necessary.

Early stage oxidation of silicon is attributed to an oxygen concentration in the ultra-pure rinse water of a few ppm [10-12]. In this work, the oxygen concentration is unknown but it is likely that this concentration exceeds the concentrations used in the references. The oxidation of the hydrogen-terminated surface can therefore occur faster if the oxygen concentration in the rinse water is higher.

The AFM picture made of a surface that is hydrogen-terminated shows features of several nanometers on the surface. Whether this is a contamination or the etching procedure did not remove all silicon oxide is unknown. On average the surface appears to be smooth and the proposed etching mechanism of silicon oxide with hydrogen fluoride appears to be valid.

From contact angle measurements, a hydrogen fluoride surface is more hydrophobic than a surface of native oxide. This increased contact angle due to hydrophobic interactions indicates the presence of hydrogen atoms of the surface. If the coverage of the surface with hydrogen is complete, is unknown. AFM measurements and contact angle measurements do not give a conclusive answer.

A sample is measured after heating from RT to 800 °C and cooling from 800 °C to RT without ramping. The value of the advancing contact angle shows that the surface re-oxidized. The exact moment in time at which the oxygen forms is unknown. From literature it is clear that the hydrogen on an etched sample evaporates at 300 °C, enters the passive oxidation regime and consecutive the active regime. When cooled from 800 °C to RT, the sample is a longer period of time in the passive oxidation regime. The equations representing the passive and active oxidation regimes have no rate constant, thus kinetics are unknown. The proposed mechanism for active silicon oxidation is based on silicon bond angle and silicon bond length calculations i.e. energy levels. Again, rate constants are unknown.

YSZ deposition

The graph in figure 5.6 should be interpreted carefully. It shows a maximum of YSZ intensities or number of counts in the silicon (001) direction. The values are normalized to the highest silicon intensity. However, other orientations can be present, which are not detected by the XRD apparatus. The TEM diffraction pattern in figure 5.7 of a sample deposited in an argon environment for 48 seconds is a good illustration, showing different orientations of YSZ besides the main (001) orientation. If an YSZ deposition of 24 seconds in an argon environment has maximum epitaxial crystalline orientation with the silicon substrate is not known.

The ‘oxygen scavenging’ theory proves to be helpful to understand the dependence on argon deposition time. TEM results are presented for samples of 24 and 48 seconds of argon environment depositions. Assuming a constant thickness of silicon oxide present prior to any deposition, a given amount of ablated YSZ in argon is needed to scavenge all silicon oxide. When this critical amount (‘argon time’ in this work) is surpassed, zirconium oxide is not able to grow epitaxially with the given PLD settings used. Assuming that non-epitaxial zirconium phases are formed but do not cover the whole surface, consecutive YSZ depositions in oxygen will have a

worse epitaxial relation. In fact the picture below representing oxygen scavenging shows the ideal situation.

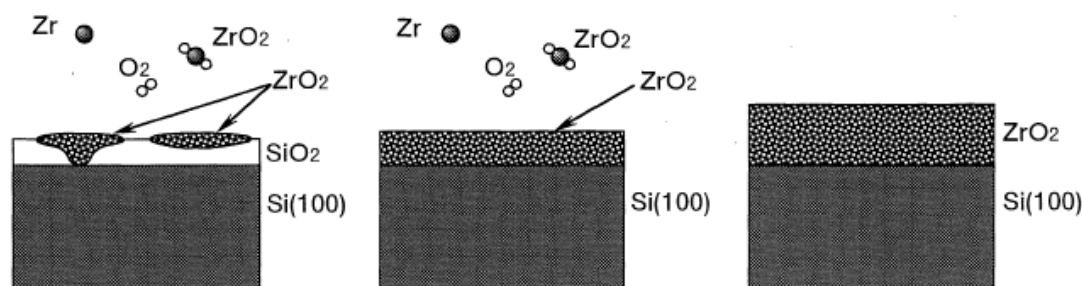


Figure 6.1: Proposed initial growth process of YSZ under $1.3 \cdot 10^{-5}$ bar oxygen pressure and $900 \text{ }^\circ\text{C}$ [4].

HREM pictures show silicon oxide thickness of 3 and 2.9 nm. If the oxygen is scavenged from the silicon surface, this silicon oxide layer should not be present. An explanation can be the ionic transport of oxygen through the YSZ lattice at elevated temperatures. When depositing at $800 \text{ }^\circ\text{C}$ YSZ in an oxygen environment it transports oxygen through its lattice towards silicon, where it re-oxidizes the silicon surface. It is also possible that during switching from an argon environment to an oxygen environment (in-situ), oxygen ions diffuse through the thin film (2-10 nm) of YSZ previously deposited in argon.

The AFM pictures show a relatively smooth surface of the deposited YSZ layers. The height differences are sufficiently small to continue deposition of electrode material.

Cerium oxide deposition

According to paragraph 3.3, coulombic interactions between an oxygen atom of silicon oxide and a cerium atom favor an (111) orientation. All measured samples presented in paragraph 5.3 show a $\text{Si}[001]//\text{CeO}_2[111]$ relation, despite variation in deposition environments. The XRD intensity of cerium oxide (111) is even highest for a sample deposited solely in an argon environment. This can indicate that coulombic interactions between ablated cerium atoms and oxygen from the silicon oxide can be assumed. If the cerium oxide possesses oxygen vacancies due to lack of oxygen has not been measured and remains unknown.

In two samples, one deposited in argon and the other in argon for one minute plus five minutes in oxygen, a cerium oxide (511) orientation is detected. One possibility for this (511) orientation is the loss of stoichiometry in cerium oxide due to lack of oxygen in the deposition environment. The phase diagram shows a delta-phase besides the stoichiometrically correct alpha phase. If this is indeed responsible for an (511) orientation is uncertain. Further information about this delta phase is lacking.

TEM measurements of an argon environment deposition of cerium oxide agree with a $\text{Si}[001]//\text{CeO}_2[001]$ relation. The small scattering of points can indicate small grains of different orientations, such as (511). In addition, the TEM picture of this sample shows a thin silicon oxide layer between silicon and cerium oxide. This supports the possibility of coulombic interactions between cerium atoms and oxygen atoms, thus influencing the crystalline orientation of cerium oxide. This picture indicates a presence of silicon oxide before starting deposition, while cerium oxide shows no 'oxygen scavenging' capabilities like YSZ.

An AFM picture of a cerium oxide layer deposited in an oxygen environment is very smooth, almost perfect to continue electrode deposition, despite the (111) orientation.

SRO deposition

The in-situ SRO deposition on an YSZ layer shows a $\text{YSZ}[001]//\text{SRO}[110]_{\text{cubic}}$ relation. This relation is the rectangle-on-cube relation as described in paragraph 3.4. The (110) plane of the pseudo cube is the (200) plane of the orthorhombic lattice in picture 3.4. The orthorhombic (200) plane is tilted 90° onto the YSZ layer. Figure 6.2 shows a schematic cross-section of this relation between YSZ and SRO. Whether strontium atoms or ruthenate atoms are responsible for the rectangle-on-cube relation is not known and cannot be concluded from literature or performed measurements.

The θ - 2θ scan in paragraph 5.4.2, figure 5.15 does not indicate a presence of crystalline cerium oxide. SRO reflections in this graph are less detectable than a Si | YSZ | SRO layer. It is plausible the cerium oxide layer was deposited amorphous onto the YSZ buffer layer. The deposition parameters could not be sufficient for an epitaxial relation between YSZ and cerium oxide. On the other hand, if cerium oxide is deposited epitaxially on YSZ, thus having a $\text{YSZ}[001]//\text{CeO}_2[001]$ relation, it is difficult to see from XRD this pattern because of the close lattice match of silicon and cerium oxide. The intensity of the silicon (004) peak is not larger than the intensity of the sample with only a deposited YSZ layer, so there should be the same number of counts for (004) planes. This agrees with the idea of an amorphous cerium oxide layer.

However, SRO partially has the (110) pseudo-cubic orientation, despite the amorphous cerium oxide layer. If this SRO (110) orientation is maybe energetically favorable or PLD settings as presented in paragraph 4 are not sufficient to grow SRO epitaxially is unknown and needs further attention.



Figure 6.2: Schematic cross-section of the rectangle-on-cube relation of SRO and YSZ.

The AFM measurement of a SRO layer deposited on YSZ shows a particular rough surface while SRO should have a layer-by-layer growth, thus having a flat surface. It is a possibility that the deposition temperature at 600°C is not sufficient to have a large enough surface mobility of atoms during deposition. No AFM data is presented of the CeO_2 | SRO sample, due to tip effects in the measurements. This problem was not solved accordingly.

Finally, (002) and (004) reflections of YSZ are clear in both XRD graphs, indicating a reproducible process for epitaxial YSZ deposition.

PZT deposition

From XRD measurements and TEM combined, PZT shows a strong epitaxial relation with SRO. This indicates that the SRO-PZT relation is not a main issue, rather the orientation of the electrode. If there is a possibility of a Si[001]//SRO[001] relation, PZT deposition should result in a Si[001]//PZT[001] relation.

Columnar growth of PZT is detected with TEM analysis and supported by an AFM measurement. This is the ordinary growth mode for PZT.

In figure 5.20, cerium oxide seems to have an epitaxial relation with YSZ, although amorphous cerium oxide was discussed earlier. Again, no peak broadening or intensifying was registered at the silicon (004) peak.

If piezoresponses of (110) oriented PZT are sufficient for device applications has not been measured.

Finally, the (002) and (004) reflections of YSZ are clear in both XRD graphs, indicating a reproducible process for epitaxial YSZ deposition

General remarks

1)

Orientation of YSZ versus the deposition time in an argon environment was performed at constant temperature (800 °C), argon gas pressure and flow (0.020 mbar, 10 ml/min), and oxygen gas pressure and flow (0.021 mbar, 10 ml/min). Laser fluency, frequency, and spot size are constant. Besides argon deposition time other dependencies were investigated, such as temperature and oxygen gas pressure (with or without a pre-deposition in argon), as well as for YSZ as for cerium oxide. In addition, the same can be applied to SRO and PZT. Unfortunately, time was not available to investigate all these parameters for different materials. Based on results that were made, changing time for deposition in argon was the most promising, especially for YSZ, since it is supported by literature. In addition, finding the ideal overall PLD settings to start YSZ experiments had to be done first. PLD settings of cerium oxide were interpreted from literature. PLD settings of SRO and PZT were copied from group members

2)

Investigating the silicon oxidation did not shed a new light on the oxidation problem. Only the presence of the silicon oxide layer is certain. One possible cause of further oxidation of the silicon surface is omitted in the discussion: At 800 °C and, before deposition, the target is pre-ablated in argon to remove contaminants. Argon gas is used to prevent (further) thermal oxidation of silicon. To avoid deposition of material during pre-ablation, a shutter is placed in the path of the plasma plume. Since all materials are oxides, there is no guarantee molecular oxygen will not be formed in the plume. It is possible that this pre-ablation even contributes to the oxidation of silicon before starting the actual deposition.

3)

The samples used are cut from a large wafer in pieces of $5 \times 5 \text{ mm}^2$. It is assumed that for this sample size the distribution of deposited material is uniform i.e. the thickness of the layer does not change throughout the sample.

7. Conclusions & Recommendations

In this work, the integration of PZT on silicon by Pulsed Laser Deposition has been studied. YSZ and cerium oxide function as buffer materials and SRO functions as electrode material. Focus was on the buffer layers, especially YSZ and its ‘oxygen scavenging’ capabilities. Related to this subject is the formation of silicon oxide on the substrate surface.

Several **conclusions** are drawn from results and discussions:

- Silicon oxide is present on sample surfaces prior to depositions. This is supported TEM analysis, which show a presence of silicon oxide in every sample. When this layer is formed during the process is unknown;
- Si[001]//YSZ[001] relation is realized. Depositing in an argon environment, followed by an oxygen deposition, can control YSZ epitaxy, depending on deposition time. In this work, a 24 seconds argon deposition shows a maximum of epitaxy. This is explained by the capability of YSZ to incorporate oxygen atoms from silicon oxide into its own lattice. This phenomenon is called ‘oxygen scavenging’. Figure 7.1 shows the argon time versus number of counts of YSZ (002) and (004) reflections, normalized to silicon reflections of the sample;
- This YSZ deposition is reproducible according to PLD settings in chapter 4;

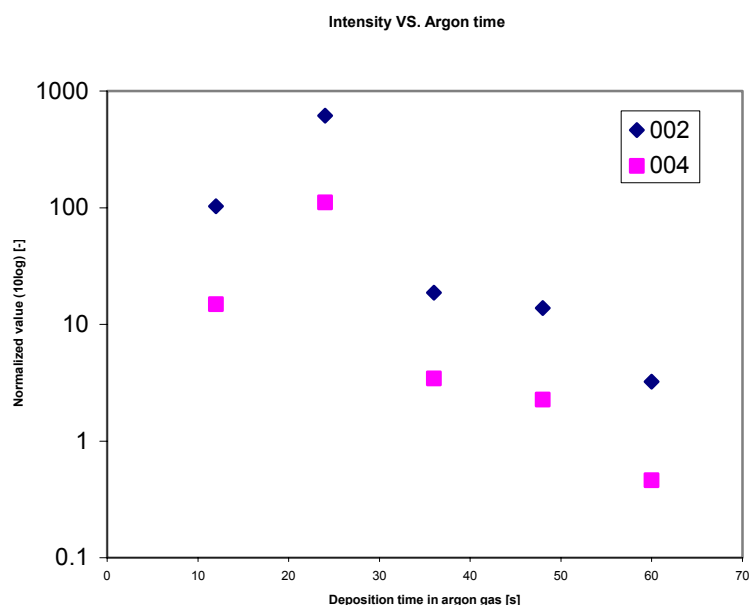


Figure 7.1: YSZ intensities normalized to silicon intensities versus deposition time of YSZ in argon gas. Diamonds represent (002) reflections of epitaxial YSZ; cubes represent (004) reflections of epitaxial YSZ. Note the logarithmic y-axis

- Si[001]//CeO₂[111] relation is influenced by oxygen stoichiometry. Interactions of silicon oxide with deposited cerium oxide are responsible for this relation;

- YSZ[001]//SRO[110]_{cubic} and SRO[110]_{cubic}//PZT[110] relations are detected. PZT shows a strong epitaxial dependence on SRO crystalline orientations;
- The realization of a Si[001]//PZT[001] relation has not been realized, rather a Si[001]//PZT[110] relation has been realized.

Based on these conclusions, **recommendations** can be made for future research.

- Silicon oxide formation on substrate surfaces should be investigated with in-situ techniques, like RHEED or in-situ AFM;
- To complete the graph in figure 7.1, more measurements should be performed.
- Piezoresponce measurements should be performed to determine if PZT (110) is suitable for actuation devices.

Dankwoord

Allereerst wil ik mijn commissie bedanken voor de inzet en de tijd die ze aan mij hebben geschonken. Guus, Arjen en Dave, bedankt voor de ‘pointers’ die ik nodig had om mijn resultaten te laten spreken, zowel tijdens besprekingen als daarbuiten. Bart Jan bedankt voor je tijd die je hebt genomen voor mijn scriptie, want tijd is immers schaars.

Ook kunnen Thang en Beatriz niet in dit rijtje ontbreken, die samen met mij een deel van MEMS-pie hebben gerealiseerd. Thang, bedankt voor alle assistentie, PLD en materiaal discussies en Champions League discussies (2004/2005, bedoel ik dan). Ik weet nu ook dat wij Nederlanders helemaal geen echte Vietnamese loempia’s op de markt eten!! Beatriz, bedankt voor de TEM plaatjes, die een belangrijk deel uitmaken van deze scriptie, zeker nu ik weet hoe ‘langweilig’ een sample prepareren kan zijn.

De studenten van de studentenkamer wil ik ook bedanken voor het in perspectief plaatsen van problemen, die je hier en daar nog wel eens boven het hoofd lijken te groeien. Eén ‘goeiesssmorgens’ of ‘hi-hiii’ is genoeg om de dag weer fris tegemoet te gaan.

Mocht ik mensen zijn vergeten te bedanken, dan doe ik dat niet omdat ik ben vergeten. Bedankt!!

Michiel Maas

Oktober 2005.

References

- [1] M.N.R. Ashfold, F. Claeysens, G.M. Fuge, S.J. Henley, 'Pulsed laser ablation and deposition of thin films', *Chem. Soc. Rev.* **33** (1) (2004) 23.
- [2] O. Auciello, R. Dat, R. Ramesh, In '*Ferroelectric thin films: synthesis and basic properties (Ferroelectricity and related phenomena; volume 10, chapter 13)*', ed. C. Paz de Araujo, J.F. Scott, G.W. Taylor, OPA B.V., Amsterdam, 1996.
- [3] D.B. Geohegan, 'Physics and diagnostics of laser ablation plume propagation for high- T_C superconductor film growth', *Thin solid films* **220** (1992) 138.
- [4] I.W. Boyd, 'Thin Film Growth by Pulsed Layer Deposition', *Ceram. Int.* **22** (1996) 429.
- [5] M. Strikovski, J.H. Miller Jr., 'Pulsed laser deposition of oxides: Why the optimum rate is about 1 Å per pulse', *Appl. Phys. Lett.* **73** (12) (1998) 1733.
- [6] C. Ratsch, J.A. Venables, 'Nucleation theory and the early stages of thin film growth', *J. Vac. Sci. Technol. A* **21** (5) (2003) S96.
- [7] J.A. Venables, G.D.T. Spiller, M. Hanbücken, 'Nucleation and growth of thin films', *Rep. Prog. Phys.* **47** (1984) 399.
- [8] D.J. Monk, D.S. Soane, R.T. Howe, 'A review of the chemical reaction mechanism and kinetics for hydrofluoric acid etching of silicon dioxide for surface micromachining applications', *Thin Solid Films* **232** (1993) 1.
- [9] J. Bühler, F.P. Steiner, H. Baltes, 'Silicon dioxide sacrificial layer etching in surface micromachining', *J. Micromech. Microeng.* **7** (1993) R1.
- [10] K. Osseo-Asare, 'Etching Kinetics of Silicon Dioxide in Aqueous Fluoride Solutions: A Surface Complexation Model', *J. Electrochem. Soc.* **143** (4) (1996) 1339.
- [11] A. Somashekhar, S. O'Brien, 'Etching SiO₂ Films in Aqueous 0.49% HF', *J. Electrochem. Soc.* **143** (9) (1996) 2885.
- [12] H. Noguchi, S. Adachi, 'Chemical treatment effects of silicon in aqueous KF solution', *Appl. Surf. Sci.* **246** (2005) 139.
- [13] K.W. Kolasinski, 'The mechanism of Si etching in fluoride solutions', *Phys. Chem. Chem. Phys.* **5** (2003) 1270.
- [14] J. Westermann, H. Nienhaus, W. Mönch, 'Oxidation stages of clean and H-terminated Si(001) surfaces at room temperature', *Surf. Sci.* **311** (1994) 101.
- [15] C.J. Sofield, A.M. Stoneham, 'Oxidation of silicon: The VLSI gate dielectric?', *Semicond. Sci. Technol.* **10** (1995) 215.

- [16] J.Qiao, C.Y. Yang, 'High- T_c superconductors on buffered silicon: materials properties and device application', *Mat. Sci. Eng. R* **14** (1995) 157.
- [17] K. Usada, K. Yamada, 'Scanning tunneling microscopy observation of hydrogen-terminated Si(001) surfaces after rinsing in ultrapure water with low dissolved oxygen concentration', *Appl. Surf. Sci.* **143** (1999) 16.
- [18] F. Li, M.K. Balazs, S. Anderson, 'Effects of ambient and dissolved oxygen concentration in ultrapure water on initial growth of native oxide on a silicon (100) surface', *J. Electrochem. Soc.* **152** (8) (2005) G669.
- [19] M. Morita, T. Ohmi, E. Hasegawa, M. Kawakami, K. Suma, 'Control factor of native oxide growth on silicon in air or in ultrapure water', *Appl. Phys. Lett.* **55** (6) (1989) 562.
- [20] N. Yabumoto, K. Saito, M. Morita, T. Ohmi, 'Oxidation Process of Hydrogen Terminated Silicon Surface Studied by Thermal Desorption Spectroscopy', *Jpn. J. Appl. Phys.* **30** (3B) (1991) L419.
- [21] F. Li, K. Balazs, B.E. Deal, 'Thickness measurement of submonolayer native oxide films on silicon wafers', *Solid State Technol.* **43** (2) (2000) 87.
- [22] T. Hattori, T. Aiba, E. Iijima, Y. Okube, H. Nohira, N. Tate, M. Katayama, 'Initial stage of oxidation of hydrogen-terminated silicon surfaces', *Appl. Surf. Sci.* **104/105** (1996) 323.
- [23] H. Kageshima, K. Shiraishi, 'Silicon-kicking-out mechanism in initial oxide formation on hydrogen-terminated silicon (001) surfaces', *Appl. Surf. Sci.* **130-132** (1998) 176.
- [24] H. Ikeda, K. Hotta, S. Furuta, S. Zaima, Y. Yasuda, 'Initial Oxidation Processes of H-terminated Si (001) surfaces studied by High-resolution electron energy loss spectroscopy', *Jpn. J. Appl. Phys.* **35** (2B) (1996) 1069.
- [25] H. Ikeda, K. Hotta, S. Furuta, S. Zaima, Y. Yasuda, 'Influences of hydrogen on initial oxidation processes of H-terminated Si(001) surfaces', *Appl. Surf. Sci.* **104/105** (1996) 354.
- [26] T. Takahagi, A. Ishitani, H. Kuroda, Y. Nagasawa, H. Ito, S. Wakao, 'Control of the chemical reactivity of a silicon single-crystal surface using the chemical modification technique', *J. Appl. Phys.* **68** (5) (1990) 2187.
- [27] T. Aiba, K. Yamauchi, Y. Shimizu, N. Tate, M. Katayama, T. Hattori, 'Initial Stage of Oxidation of Hydrogen-Terminated Si(100)- 2×1 Surface', *Jpn. J. Appl. Phys.* **34** (1995) 707.
- [28] B.E. Deal, A.S. Grove, 'General Relationship for the Thermal oxidation of silicon', *J. Appl. Phys.* **36** (12) 3770, (1965).

- [29] N. Cabrera, N.F. Mott, 'Theory of the oxidation of metals', *Rep. Prog. Phys.* **12** 163, (1948-1949).
- [30] P.J. Jorgensen, 'Effect of an Electric Field on Silicon Oxidation', *J. Chem. Phys.* **37** (4) 874, 1962.
- [31]] A. Atkinson, 'Transport processes during the growth of oxide films at elevated temperature', *Rev. Mod. Phys.* **52** (2) 437, (1985).
- [32] C.H. Choi, D-J. Liu, J.W. Evans, M.S. Gordon, 'Passive and active oxidation of Si(001) by Atomic Oxygen: A Theoretical Study of possible reactions Mechanisms', *J. Am. Chem. Soc.* **124** (2002) 8730.
- [33] D. Starodub, E.P. Gusev, E. Garfunkel, T. Gustafsson, 'Silicon oxide decomposition and desorption during the thermal oxidation of silicon', *Surf. Rev. Lett.* **6** (1999) 45.
- [34] Q. Li, S.J. Wang, P.C. Lim, J.W. Chai, A.C.H. Huan, C.K. Ong, 'The decomposition mechanism of SiO₂ with the deposition of oxygen-deficient M(Hf or Zr)O_x films', *Thin Solid Films* 462-463 (2004) 106.
- [35] D.K. Fork, D.B. Fenner, G.A.N. Connell, J.M. Philips, T.H. Geballe, 'Epitaxial yttria-stabilized zirconia on hydrogen-terminated Si by pulsed laser deposition', *Appl. Phys. Lett.* **57** (11) (1990) 1137.
- [36] A. Bardal, Th. Matthée, J. Wecker, K. Samwer, 'Initial stages of epitaxial growth of Y-stabilized ZrO₂ thin films on *a*-SiO_x/Si(001) substrates', *J. Appl. Phys.* **75** (6) (1994) 2902.
- [37] T. Hirai, K. Teramoto, H. Koike, K. Nagashima, Y. Tarui, 'Initial stage and growth process of ceria, yttria-stabilized-zirconia and ceria-zirconia mixture thin films on Si(001) surfaces', *Jpn. J. Appl. Phys.* **36** (1997) 5253.
- [38] S. Kaneko, K. Akiyama, Y. Shimizu, T. Ito, S. Yasaka, M. Mitsuhashi, S. Ohya, K. Saito, T. Watanabe, S. Okamoto, H. Funakubo, 'Effect of buffer layer on epitaxial growth of YSZ deposited on Si substrate by slower Q-switched 266 nm laser', *Jpn. J. Appl. Phys.* **43** (4A) (2004) 1532.
- [39] S.J. Wang, S.Y. Xu, L.P. You, S.L. Lim, C.K. Ong, 'Microstructural studies on a high quality Yba₂Cu₃O_{7-δ}/YSZ/Si multiplayer prepared by pulsed-laser deposition', *Supercond. Sci. Technol.* **13** (2000) 362.
- [40] S.Y. Chow, S. Wang, 'The partial pressure effect on the growth of YSZ film and YSZ buffered multilayers on silicon', *Ceram. Int.* **30** (2004) 1257.
- [41] D.B. Fenner, A.M. Viano, D.K. Fork, G.A.N. Conell, J.B. Boyce, F.A. Ponce, J.C. Tramontana, 'Reactions at the interfaces of thin films of Y-Ba-Cu- and Zr-oxides with Si substrates', *J. Appl. Phys.* **69** (4) (1991) 2176.

- [42] T. Kiguchi, N. Wakiya, K. Shinozaki, N. Mizutani, 'High-temperature in situ cross-sectional transmission electron microscopy investigation of crystallization process of yttrium-stabilized zirconia/Si and yttrium-stabilized zirconia/SiO_x/Si thin films', *J. Mater. Res.* **20** (7) (2005) 1878.
- [43] M. Yoshimoto, H. Nagata, T. Tsukahara, H. Koinuma, '*In Situ* observation of CeO₂ film growth on Si by laser ablation deposition in ultrahigh-vacuum', *Jpn. J. Appl. Phys.* **29** (7) (1990) L1199.
- [44] H. Nagata, T. Tsukahara, S. Gonda, M. Yoshimoto, H. Koinuma, 'Heteroepitaxial growth of CeO₂ (001) films on Si(001) substrates by pulsed laser deposition in ultrahigh vacuum', *Jpn. J. Appl. Phys.* **30** (6B) (1991) L1136.
- [45] T. Inoue, T. Ohsuna, L. Luo, X.D. Wu, C.J. Maggiore, Y. Yamamoto, Y. Sakurai, J.H. Chang, 'Growth of (110)-oriented CeO₂ layers on (100) silicon substrates', *Appl. Phys. Lett.* **59** (27) (1991) 3604
- [46] T. Ami, I. Ishida, N. Nagasawa, A. Machida, M. Suzuki, 'Room-temperature epitaxial growth of CeO₂ (001) thin films on Si(001) substrates by electron beam evaporation', *Appl. Phys. Lett.* **78** (10) (2001) 1361.
- [47] J. Kang, X. Liu, G. Lian, Z. Zhang, G. Xiong, X. Guan, R. Han, Y. Wang, 'Crystal-orientation controlled epitaxial CeO₂ dielectric thin films on Si(001) substrates using pulsed laser deposition', *Microelectron. Eng.* **56** (2001) 191.
- [48] M. Li, Z. Wang, G. Xiong, S. Fan, Q. Zhao, K. Lin, 'Epitaxial growth characteristics of oxide thin films prepared by pulsed laser deposition', *Thin Solid Films* **375** (2000) 271.
- [49] Y-M. Wu, J-T Lo, 'Dielectric properties of PbTiO₃ thin films on CeO₂/Si(001) and Y₂O₃/Si(100)', *Jpn. J. Appl. Phys.* **37** (1998) 5645.
- [50] Gmelin Handbuch der anorganischen Chemie, Verlag Chemie, Berlin, 1924-...
- [51] A.J.H.M. Rijnders, 'The initial growth of complex oxides: study and manipulation', PhD thesis, University of Twente, Enschede, 2001, ISBN: 90-365-1657-9.
- [52] S.Y. Hou, J. Kwo, R.K. Watts, J-Y. Cheng, D.K. Fork, 'Structure and properties of epitaxial Ba_{0.5}Sr_{0.5}TiO₃/SrRuO₃/ZrO₂ heterostructure on Si grown by off-axis sputtering', *Appl. Phys. Lett.* **67** (10) (1995) 1387.
- [53] X. Zhu, S.K. Lee, H.N. Lee, D. Hesse, 'Microstructure of (110)-oriented epitaxial SrRuO₃ thin films grown on off-cut single crystal YSZ(100) substrates', *Mater. Sci. Eng. B* **118** (2005) 60.
- [54] H.N. Lee, S. Senz, A. Visinoiu, A. Pignolet, D. Hesse, U. Gösele, 'Epitaxial growth of non-c-oriented ferroelectric SrBi₂Ta₂O₉ thin films on Si(100) substrates', *Appl. Phys. A* **71** (2000) 101.

- [55] H.N. Lee, S. Senz, N.D. Zakharov, C. Harnagea, A. Pignolet, D. Hesse, U. Gösele, 'Growth and characteristics of non-c-oriented epitaxial ferroelectric SrBi₂Ta₂O₉ films on buffered Si(100)', Appl. Phys. Lett. **77** (20) (2000) 3260.
- [56] B. Noheda, J.A. Gonzalo, L.E. Cross, R. Guo, S-E. Park, D.E. Cox, G. Shirane, 'Tetragonal-to-monoclinic phase transition in a ferroelectric perovskite: The structure of PbZr_{0.52}Ti_{0.48}O₃', Phys. Rev. B **61** (13) (2000) 8687.
- [57] http://www.msm.cam.ac.uk/Teaching/PtIII/M7/M7_handout_22-351.pdf
- [58] D. Damjanovic, 'Ferroelectric, dielectric and piezoelectric properties of ferroelectric thin films and ceramics', Rep. Prog. Phys. **61** (1998) 1267.